Supplementary Information (SI) for Chemical Science.
This journal is © The Royal Society of Chemistry 2024

Supporting Information

Asymmetric Rh-O-Co bridge sites enable superior bifunctional catalysis for hydrazine-assisted hydrogen production

Jinrui Hu,[#a] Xuan Wang,[#a] Yi Zhou,[a] Meihan Liu,[a] Caikang Wang,[a] Meng Li,[a] Heng Liu,[b] Hao Li,[b] Yawen Tang,*[a] Gengtao Fu*[a]

[a] Jiangsu Key Laboratory of New Power Batteries, Jiangsu Collaborative Innovation Center of Biomedical Functional Materials, School of Chemistry and Materials Science, Nanjing Normal University, Nanjing 210023, China
E-mail: tangyawen@njnu.edu.cn (Y. Tang); gengtaofu@njnu.edu.cn (G. Fu)

[b] Advanced Institute for Materials Research (WPI-AIMR), Tohoku University, Sendai 980-8577, Japan

[#] These authors contributed equally to this work.

Experimental

Reagents and chemicals

Cobalt(II) nitrate hexahydrate ($Co(NO_3)_2 \cdot 6H_2O$), arginine ($C_6H_{14}N_4O_2$), hydrazine monohydrate ($N_2H_4 \cdot H_2O$) and ethylene glycol (EG) were purchased from Aladdin Chemistry Co., Ltd (Shanghai China). The 20% Pt/C was purchased from Johnson Matthey Corporation. Rhodium(III) Chloride Hydrate ($RhCl_3 \cdot nH_2O$) was purchased from D&B Biological Science and Technology Co., Ltd (Shanghai China). Ethanol (C_2H_5OH) was purchased from Sinopharm Chemical Reagent Co., Ltd (Shanghai, China). All the reagents were of analytical reagent grade and used without further purification.

Synthesis of Co_3O_4 BNSs

Typically, 300 mg of arginine and 291 mg of $Co(NO_3)_2$ were dissolved in 28 mL of deionized (DI) water and 7 mL of ethanol by sonication and stirred for 1 h. Then, the prepared solution was transferred into a 50 mL Teflon-lined stainless-steel autoclave, which was maintained at 160 °C for 5 h before cooling down to room temperature. The solution was centrifuged and washed three times with a mixed solution of ethanol and DI, and freeze-dried to obtain the Co_3O_4 BNSs.

Synthesis of Rh-Co_3O_4 BNSs

For the synthesis of Rh-Co_3O_4 BNSs ($Rh_{15.1\ wt\%}$-Co_3O_4 BNSs), 50 mg of Co_3O_4 BNSs was dissolved in 50 mL of EG and ultrasound for 10 min. Then 1.2 mL of $RhCl_3 \cdot nH_2O$ aqueous solution (20 mg mL^{-1}) was dropwise added to the above mixture under strong stirring. After stirring for 2 h, the obtained mixture was heated to 160 °C and refluxed for 3 h. The Rh-Co_3O_4 BNSs was obtained by washing three times and drying again. While keeping other experimental conditions and the mass of the Co_3O_4 BNSs precursor unchanged, the $RhCl_3 \cdot nH_2O$ solution changed to 0.6 mL and 1.8 mL respectively, for obtaining the $Rh_{7.9\ wt\%}$-Co_3O_4 BNSs and $Rh_{31.7\ wt\%}$-Co_3O_4 BNSs.

Physicochemical characterization

The crystal phase of catalysts was investigated by X-ray powder diffraction (XRD) on a D/max-rC X-ray diffractometer (Cu Kα radiation, λ = 1.5406 Å). Scanning electron microscopy (SEM) and transmission electron microscopy (TEM) images were obtained using a JEOL JSM7500F and a HITACHI 7800 (with an accelerating voltage of 80 kV), respectively. High-resolution transmission

electron microscopy (HRTEM), high-angle annular dark-field scanning transmission electron microscopy (HAADF-STEM), and energy-dispersive X-ray spectroscopy (EDX) were acquired on a JEOL JEM-2100F with accelerating voltages of 200 kV. Ultraviolet and visible spectroscopy (UV–vis) spectra were measured usig a UV-670 spectrophotometer produced by MAPYDA. X-ray photoelectron spectroscopy (XPS) data were obtained on Thermo VG Scientific ESCALAB 250 spectrometer with an Al Kα light source. The synchrotron-based X-ray absorption spectroscopy (XAS) was measured at the beamline 1W1B station of Beijing Synchrotron Radiation Facility (BSRF). The XAS spectra were analysed using the ATHENA software package, with a Fourier transform in the k-range of 3 to 10 and a window function of Hanning. The wavelet transform was performed using k-space with a k-weight of 2. Electron paramagnetic resonance (EPR) data were obtained on Bruker A300-10 at 77 K. In situ Raman spectra were recorded on a Raman spectrometer (Lab RAM HR800) at the radiation wavelength of 532 nm.

Electrochemical Measurements

All electrochemical tests were conducted at room temperature (25°C) using a CHI 760E electrochemical analyzer in a three-electrode configuration. A glassy carbon electrode (GCE, d = 3 mm) coated with catalyst ink was used as the working electrode, a saturated calomel electrode (SCE) served as the reference electrode, and a graphite rod was employed as he counter electrode. To fabricate the working electrode, 4 mg of catalyst and 1 mg of Vulcan XC-72 carbon were dispersed in a mixture of 0.5 mL ethanol and 0.5 mL water. The resulting dispersion was homogenized by sonication to form a uniform ink. Subsequently, 5 μL of the catalyst ink was applied to the surface of the GCE in two sequential additions, each followed by drying. Finally, 3 μL of 20% Nafion solution was added, and the electrode was dried to complete the fabrication of the working electrode. All electrode potentials measured using a SCE as the reference electrode were converted to reversible hydrogen electrodes (RHE) according to the following equation: $E_{(RHE)} = E_{(SCE)} + 0.059\ pH + 0.242$. The Tafel slope was calculated according to the Tafel equation as follows: $\eta = b\log(j/j_0)$, where η denotes the overpotential, b denotes the Tafel slope, j denotes the current density, and j_0 denotes the exchange current density.

Hydrogen evolution reaction (HER) was conducted in a N_2-saturated 0.5 M H_2SO_4 solution. Linear sweep voltammetry (LSV) curves were performed at a sweep rate 5 mV s^{-1}, with all data corrected for *iR* losses. The overpotential (η) was calculated with following equation: $\eta = E_{RHE} - 0$ V.

Electrochemical impedance spectroscopy (EIS) plots were conducted at the potential of 10 mA cm^{-2} (E_{10}) over a scanning frequency range from 100 kHz to 0.01 Hz. The electrochemical double-layer capacitance (C_{dl}) was obtained by a series of CV tests (scan rate 20 to 100 mV s^{-1}) in the potential range of -0.02 to 0.08V (vs. RHE). The accelerated durability test (ADT) was conducted in the potential range from −0.08 to 0.02 V vs. RHE at a scan rate of 100 mV s^{-1}. Long-term stability was assessed by chronopotentiometry at a current density of 10 mA cm^{-2} for 20 h. The Faradaic yield was calculated from the total charge Q (C) passed through the cell and the total amount of oxygen produced n (mol). Theoretically, the production of 0.38 ml of hydrogen at a current of 20 mA would take approximately 300 seconds (the molar volume of gas is 24.5 L mol^{-1} at 25 °C).

Hydrazine oxidation reactions (HzOR) and oxygen evolution reaction (OER) were performed in N_2-saturated 0.5 M H_2SO_4 + 0.05 M N_2H_4 solution and O_2-saturated 0.5 M H_2SO_4 solution, respectively. The LSV curve sweeps were recorded at a scan rate of 5 mV s^{-1} , with the data corrected for *iR* losses. For HzOR, the chronoamperometric curves tracked the decay of current from 10 mA cm^{-2} over 20 h. The ADT was conducted in the potential range from 0.21 to 0.31 V vs. RHE at a scan rate of 100 mV s^{-1}.

Overall water splitting (OWS) and overall hydrazine splitting (OHzS) were conducted in a two-electrode configuration comprising a 0.5 M H_2SO_4 solution and a 0.5 M H_2SO_4 + 0.05 M N_2H_4 solution as the electrolyte, respectively. Both cathode and anode comprised carbon cloth (active area of 1*1 cm^2) coated with 100 uL of catalyst ink. LSV curves were performed at a rate of 5 mV s^{-1} and corrected for *iR* losses. Chronoamperometric curves also recorded the decay of current from 10 mA cm^{-2} over 20 h.

In situ Raman measurements

To monitor the electrochemical conversion of Rh-Co_3O_4 BNSs in real-time during the HzOR process, an inverse Raman spectroscopy setup, integrating a Labram HR800 and a 532 nm laser, was employed. In situ Electrochemical Surface-Enhanced Hyper-Raman Scattering (EC-SHINERS) was performed using this setup along with a CHI 760E electrochemical workstation. The Raman cell used in the experiment was obtained from Beijing Scistar Technology Co. Ltd. It was equipped with a (Au@SiO_2)@VP/CNs-modified GCE as the working electrode, a Pt wire as the counter electrode, and an Ag/AgCl (saturated KCl) electrode as the reference. The electrode potentials in in situ Raman tests

were converted to the reversible hydrogen electrode (RHE) scale using the equation: $E_{(RHE)} = E_{(Ag/AgCl)} + 0.059\ pH + 0.197$. Both Rh-$Co_3O_4$BNSs and Co_3O_4 BNSs were tested at the potentials ranging from 0.05 to 0.25 V vs. RHE in a 0.05 M H_2SO_4 + 0.05 M N_2H_4 electrolyte solution.

Theoretical Calculations

All the spin-polarized density functional theory (DFT) calculations were performed *via* Vienna *ab initio* Simulation Package[1-3] (VASP) with the use of projector augmented-wave (PAW) method[4, 5]. The exchange-correlation (XC) term in Kohn-Sham DFT equation was described by revised Perdew-Burke-Ernzerhof (RPBE) by Nørskov et al.[6] under the generalized gradient approximation (GGA) framework. The wavefunction in Kohn-Sham DFT equation was expanded using plane-wave basis sets with energy cutoff of 400 eV, which is accompanied by Gaussian smearing method with sigma value of 0.05 eV around the Fermi level. For pseudopotentials, the Rh $4d^85s^1$, Co $3d^84s^1$, and O $2s^22p^4$ were treated as valence electrons. To describe the van deer Waals correction, the D3 dispersion term proposed by Grimme et al.[7] with Becke-Johnson (BJ) damping was added upon RPBE as RPBE-D3(BJ). To deal with the strongly on-site coulombic interaction from localized 3d and 4d electrons, the Hubbard U correction by Dudarev et al.[8] was introduced by considering the effective U value (U_{eff}), where 4.4, 6.7, and 2.0 eV were adopted for Co (T_d)-3d, Co(O_h)-3d, and Rh-4d electrons, respectively.[9-11] For geometric optimization, the force and energy convergence threshold were 0.02 eV/Å and 10^{-5} eV, respectively. The first Brillouin-zone k-points sampling for bulk Co_3O_4 structure was 4 × 4 × 4. According to previous work, the typical active surface of spinel oxide for OER was (001) surface, so in this model, we mainly concentrated on the (001) surface of Co_3O_4. For construction of slab model, the vacuum layer was set to 15 Å to avoid the periodic self-interaction along the z-direction.

To describe the HER process, H^+/e^- was treated by the computational hydrogen electrode (CHE) model proposed by Nørskov et al.[12] The free energy of H^+/e^- equals to 0.5 G(H_2, g) at standard hydrogen electrode (SHE) condition (U_{SHE} = 0, pH = 0). At T = 298.15 K and p = 0.035 bar, the free energy of H_2O(l) can be replaced by G(H_2O, g). G(H_2O, g) can be calculated by the H_2O molecule in a periodic box. Free energy of O_2 can be indirectly calculated by referring to $2H_2(g) + O_2(g) \rightarrow 2H_2O(l)$ as $G(O_2) = 2G(H_2O, l) - 2G(H_2) + 4.92$ eV. For each oxygen intermediate, the free energy can be calculated as G = E + ZPE – TS, where E stands for the total energy, ZPE is the zero-point energy, T

is the absolute temperature, and S represents the entropy. The bias potential acted on the free energy of e^- can be treated as $\Delta G(U) = - eU_{RHE}$, where U_{RHE} is the electrode potential versus reversible hydrogen electrode (RHE).

Surface Pourbaix diagrams[13] were investigated to unveil the realistic surface state by functioning electrode potential and pH effect. To be specific, various electrochemical intermediates were included: *OH, *O, and *H. The different monolayer (ML) coverages of these intermediates were determined in equilibrium with H_2O and H^+/e^- *via* $xH_2O + * \rightarrow *O_xH_y + (2x - y)(H^+ + e^-)$:

$$\Delta G = G(*O_xH_y) + (2x - y)[0.5G(H_2) - eU_{RHE}] - xG(H_2O) - G(*)$$

Figures and Tables

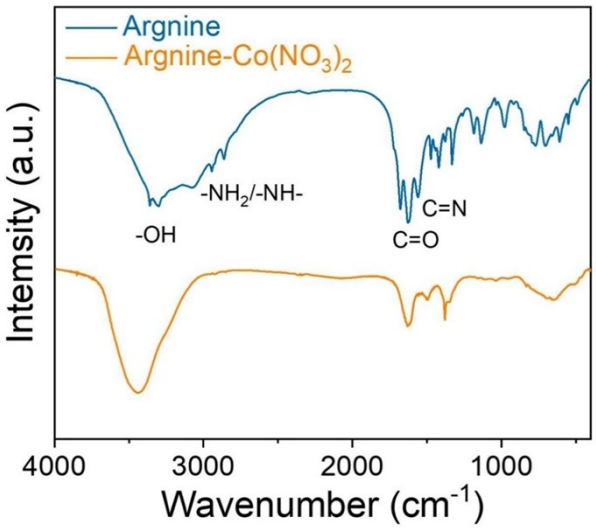

Figure S1. FTIR measurements of argnine-$Co(NO_3)_2$ and argnine.

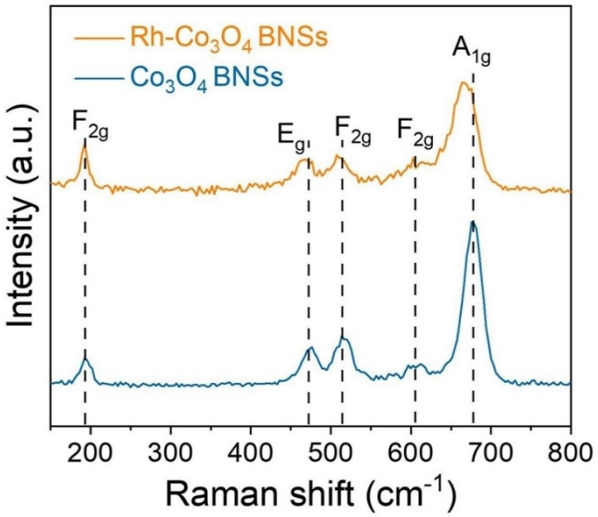

Figure S2. Raman spectra of Rh-Co_3O_4 BNSs and Co_3O_4 BNSs.

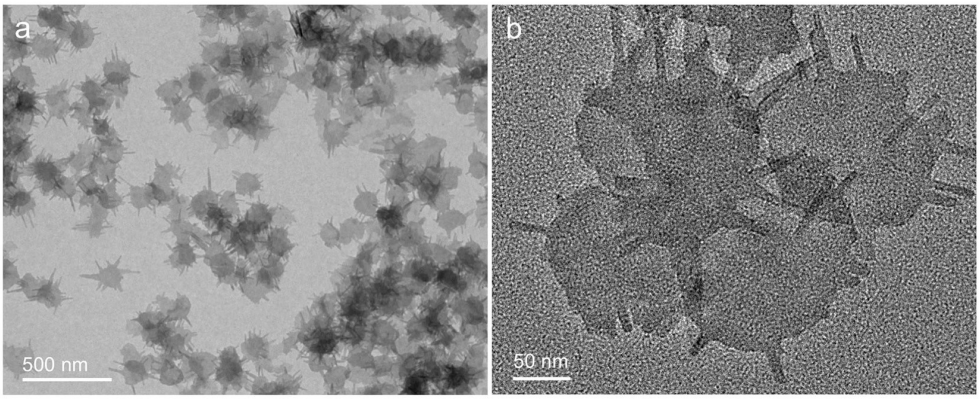

Figure S3. TEM images of Co_3O_4 BNSs.

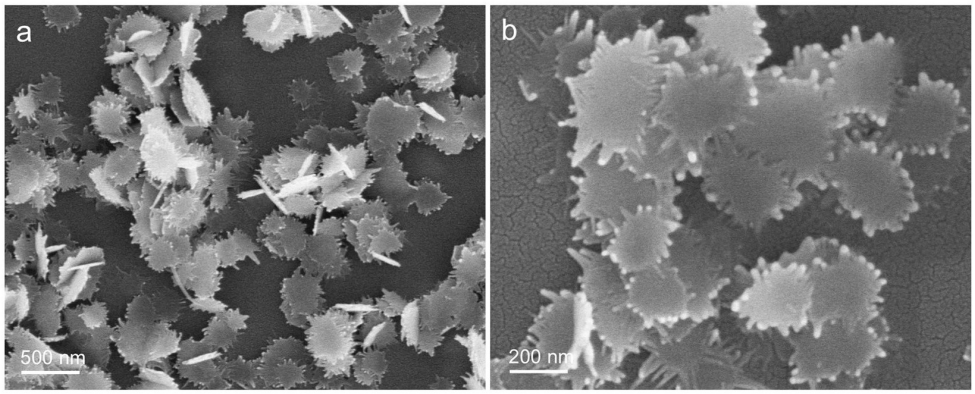

Figure S4. SEM images of Co_3O_4 BNSs.

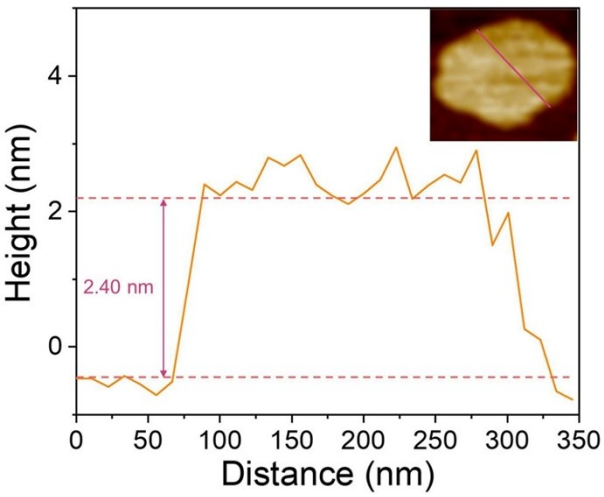

Figure S5. AFM image of Co_3O_4 BNSs

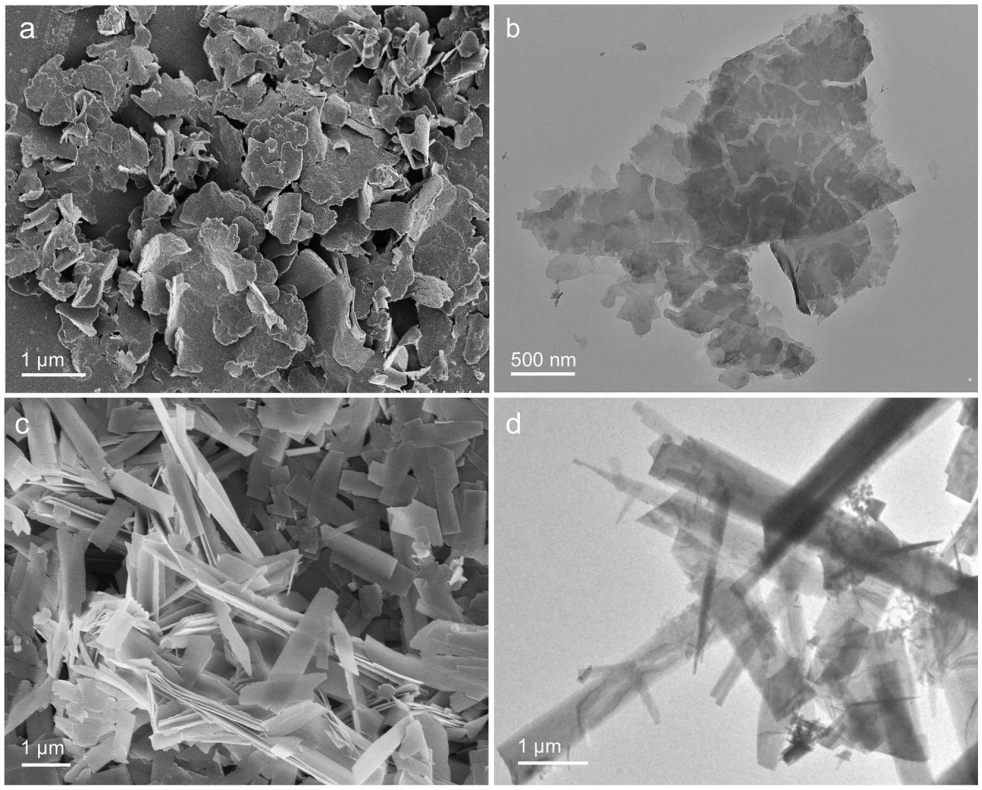

Figure S6. (a) SEM and (b) TEM images of Co_3O_4 synthesized in the absence of arginine; (c) SEM and (d) TEM images of Co_3O_4 synthesized at a high amount of arginine (600 mg).

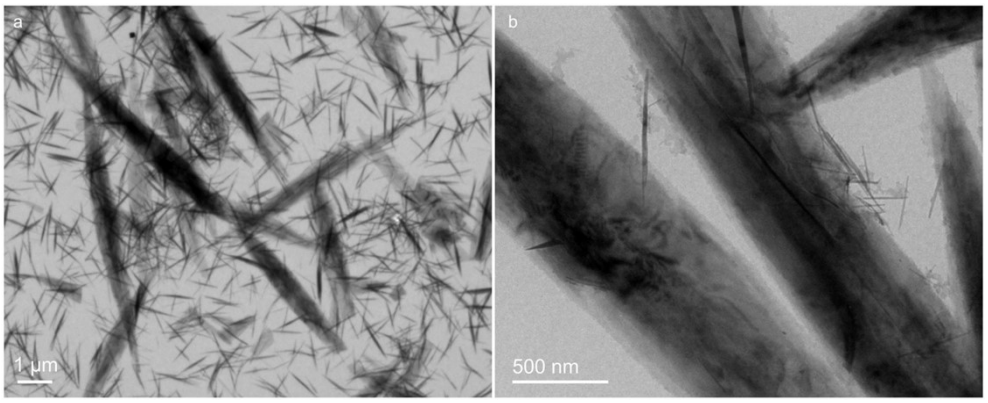

Figure S7. TEM images of the precursor prepared in pure water.

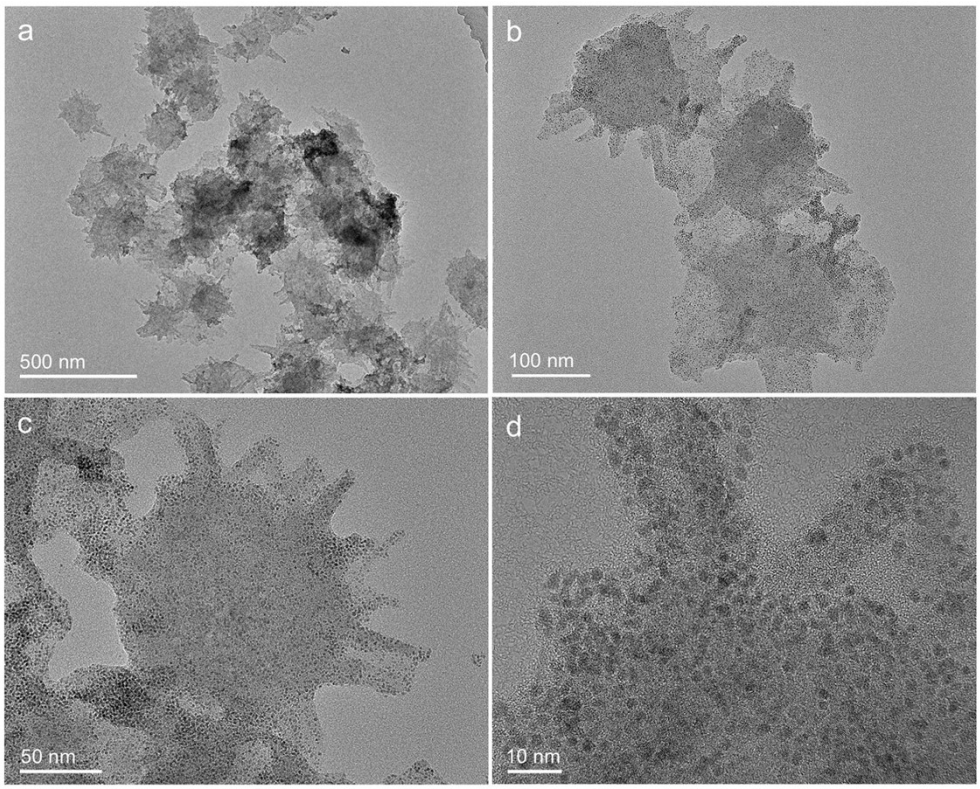

Figure S8. TEM images of Rh-Co_3O_4 BNSs with different resolutions.

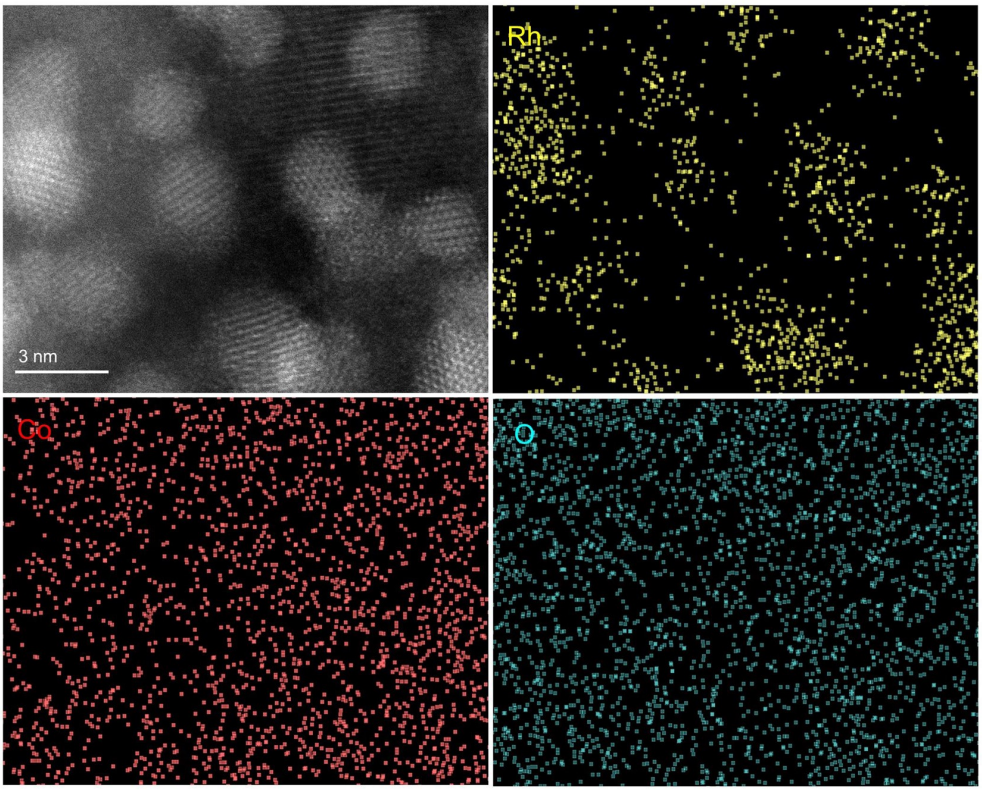

Figure S9. EDX element mapping images of Rh-Co_3O_4 BNSs in the locally magnified region.

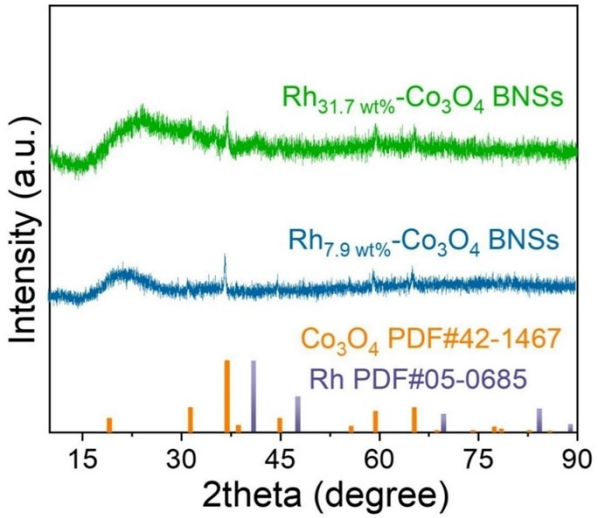

Figure S10. XRD patterns of $Rh_{7.9\ wt\%}$-Co_3O_4 BNSs and $Rh_{31.7\ wt\%}$-Co_3O_4 BNSs.

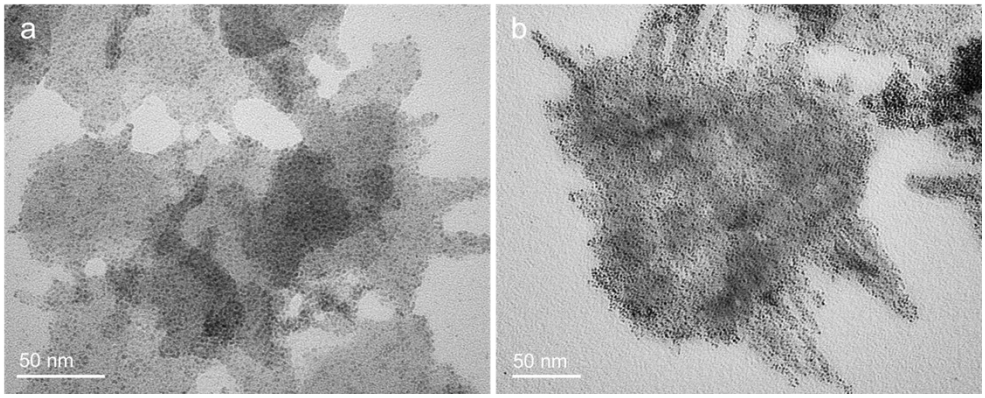

Figure S11. TEM images of (a) $Rh_{7.9\ wt\%}$-Co_3O_4 BNSs and (b) $Rh_{31.7\ wt\%}$-Co_3O_4 BNSs.

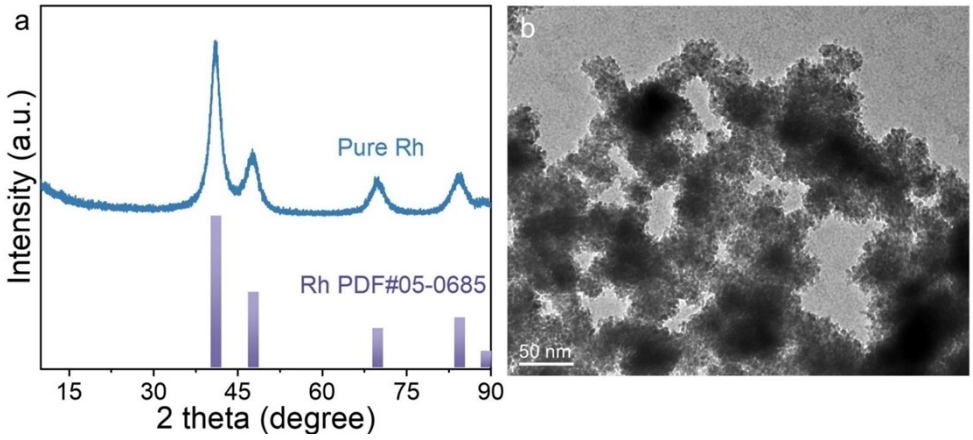

Figure S12. (a) XRD pattern and (b) TEM image of pure Rh.

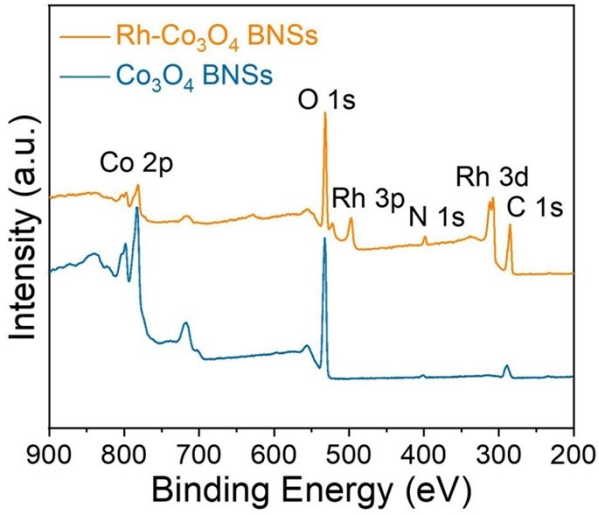

Figure S13. Full XPS spectra of Rh-Co_3O_4 BNSs and Co_3O_4 BNSs.

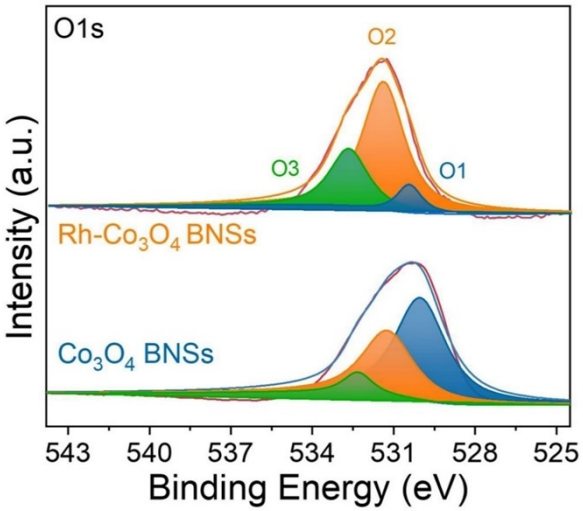

Figure S14. High-resolution O 1s XPS spectra of Rh-Co_3O_4 BNSs and Co_3O_4 BNSs.

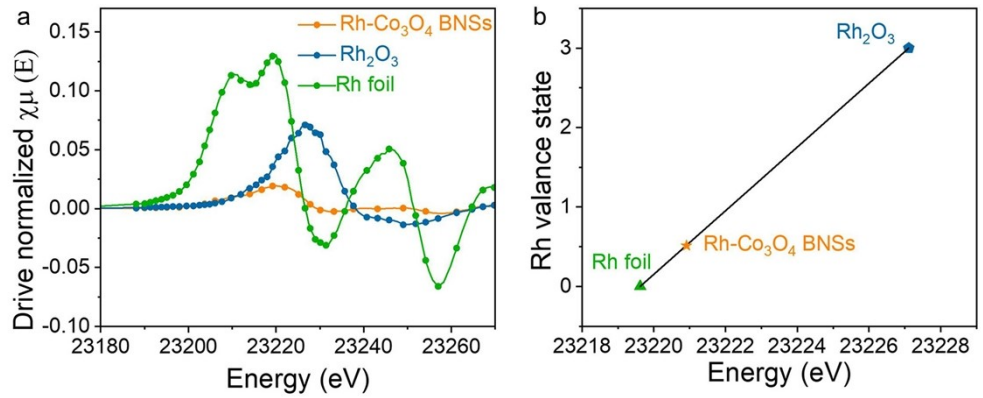

Figure S15. (a) Absorption threshold energy of Rh K-edge; (b) Calculated valence states of Rh electrocatalysts.

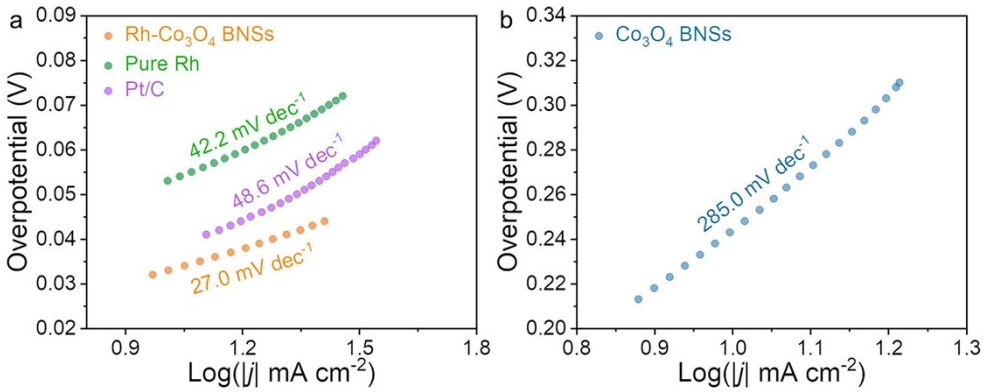

Figure S16. (a) Tafel slope of Rh-Co_3O_4 BNSs, pure Rh, Pt/C and (b) Co_3O_4 BNSs.

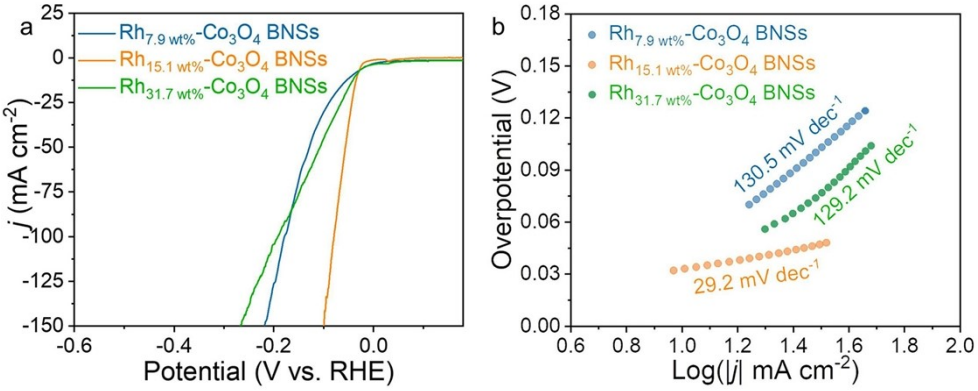

Figure S17. (a) HER polarization curves and (b) the corresponding Tafel slope of $Rh_{7.9\ wt\%}$-Co_3O_4 BNSs, $Rh_{15.1\ wt\%}$-Co_3O_4 BNSs and $Rh_{31.7\ wt\%}$-Co_3O_4 BNSs.

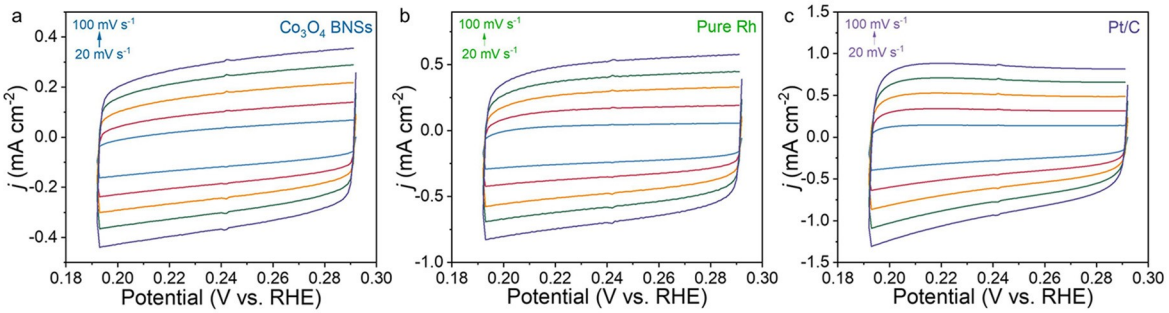

Figure S18. CV curves obtained for (a) Co_3O_4 BNSs, (b) pure Rh and (c) Pt/C in 0.5 M H_2SO_4 at different scanning rates from 20 to 100 mV s^{-1}.

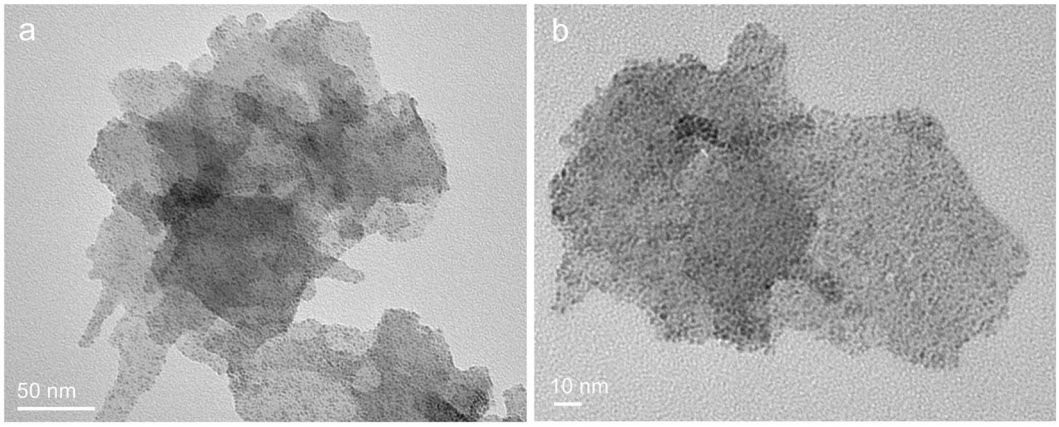

Figure S19. TEM images of of Rh-Co_3O_4 BNSs after the HER stability test.

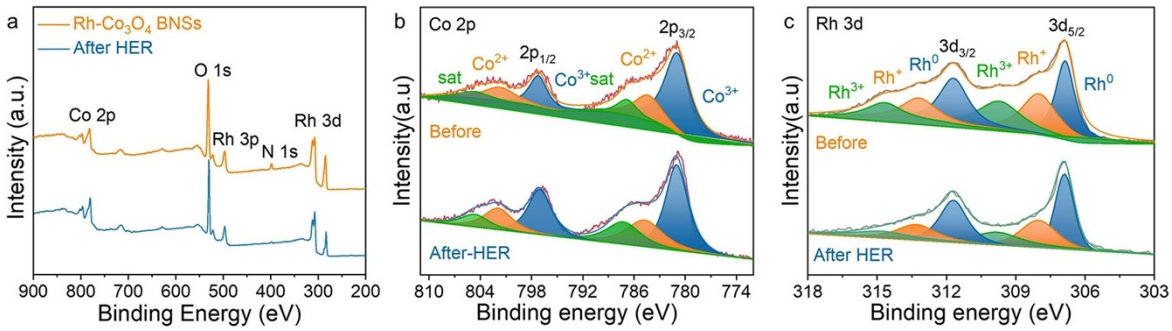

Figure S20. (a) Full XPS spectra, (b) Co 2p XPS spectra, and (c) Rh 3d XPS spectra after HER stability.

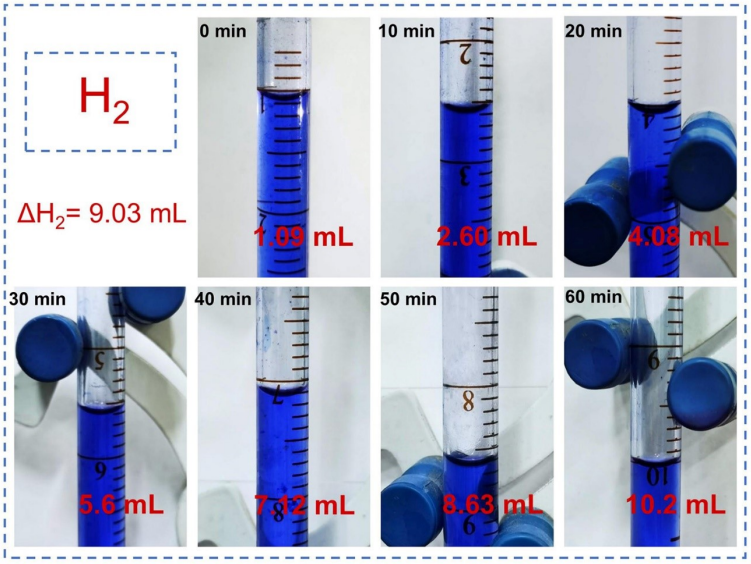

Figure S21. The volume change of produced H_2 obtain from the drainage method.

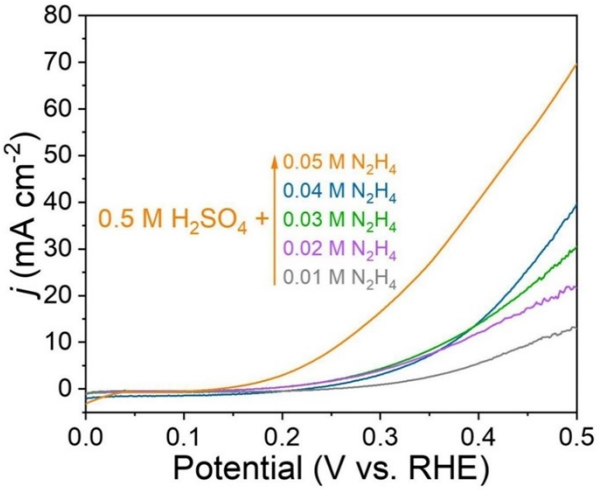

Figure S22. Polarization curves of Rh-Co_3O_4 BNSs with different concentrations of hydrazine.

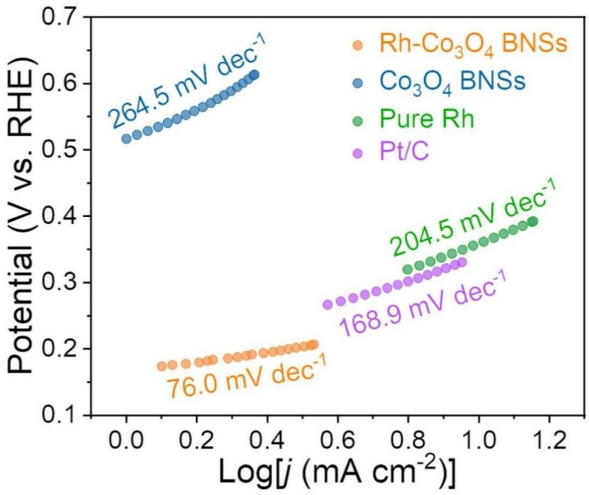

Figure S23. Tafel slope of Rh-Co_3O_4 BNSs, Co_3O_4 BNSs, pure Rh and Pt/C recorded from HzOR polarization curves.

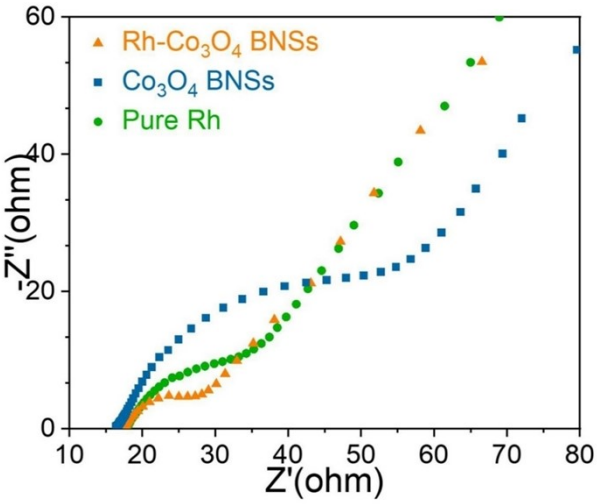

Figure S24. EIS Nyquist plots of HzOR.

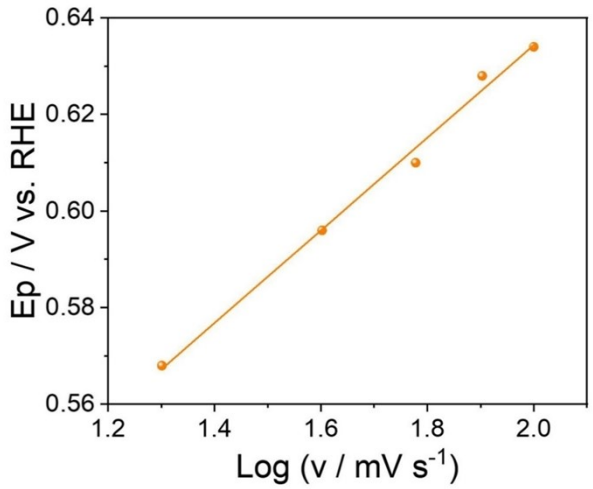

Figure S25. E_p vs. log(ν) plot from Figure 5d.

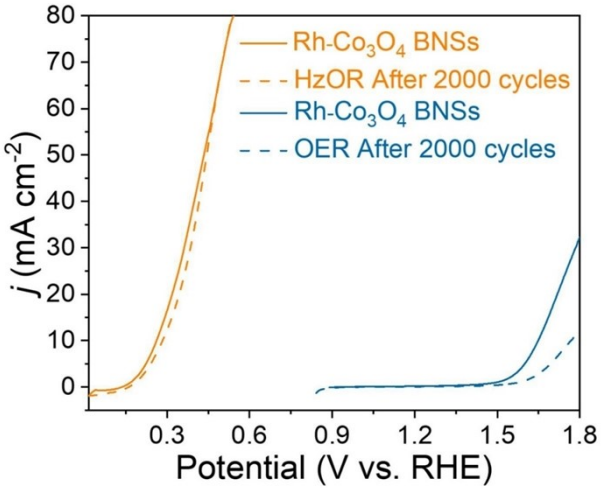

Figure S26. HER polarization curves of Rh-Co_3O_4 BNSs in 0.5 M H_2SO_4 with and without 0.05 M N_2H_4.

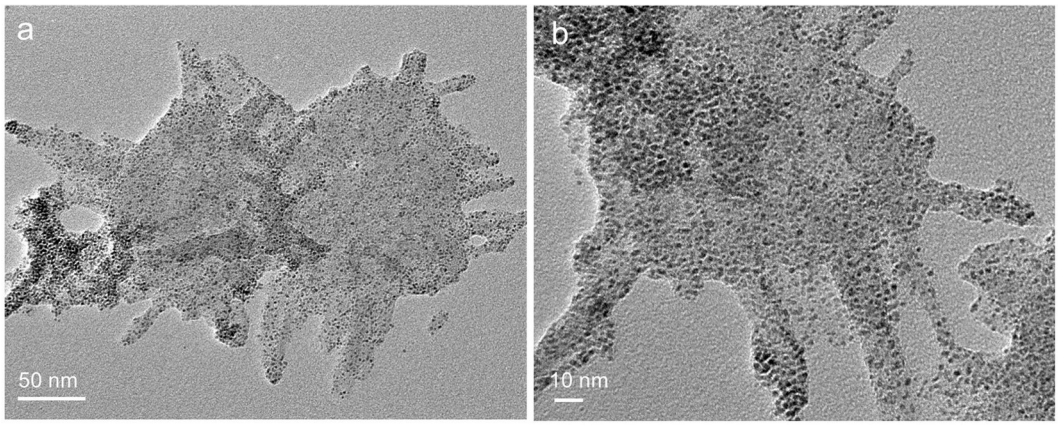

Figure S27. TEM images of of Rh-Co3O4 BNSs after the HzOR stability test.

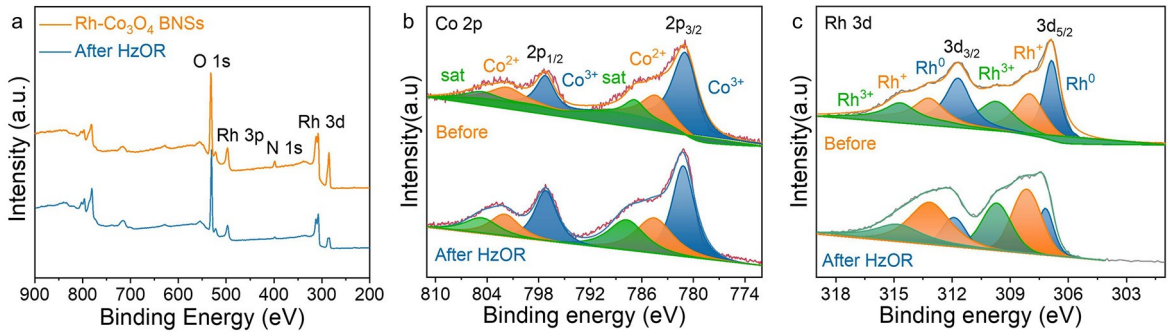

Figure S28. (a) Full XPS spectra, (b) Co 2p XPS spectra, and (c) Rh 3d XPS spectra after HzOR.

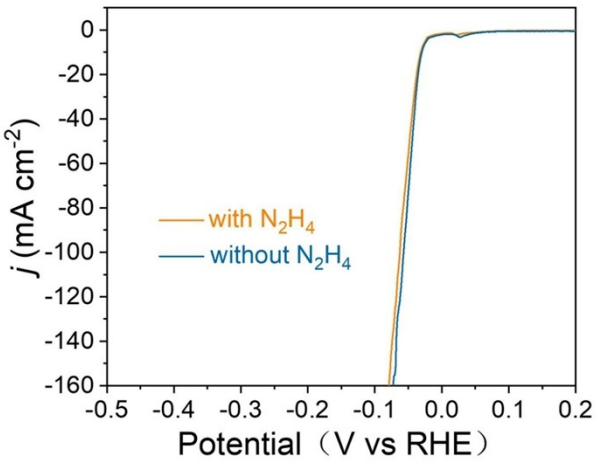

Figure S29. HER polarization curves of Rh-Co_3O_4 BNSs in 0.5 M H_2SO_4 with and without 0.05 M N_2H_4.

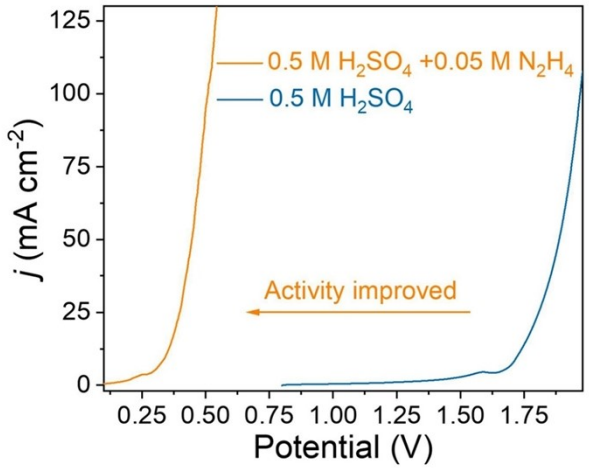

Figure S30. Polarization curves fo OHzR in 0.5 M H_2SO_4 + 0.05 M N_2H_4 and OWS in 0.5 M H_2SO_4.

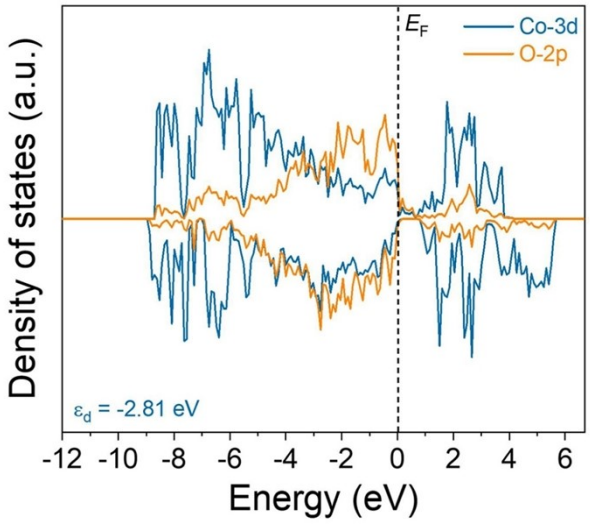

Figure S31. PDOS of Co_3O_4 (100).

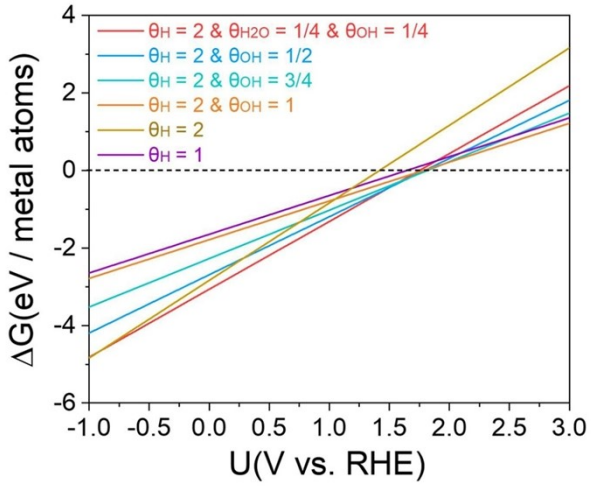

Figure S32. Calculated surface Pourbaix diagram at 25 °C and pH = 0.

Table S1. Comparison of HER activity of catalysts with reported catalysts.

Catalyst	Electrolyte	Overpotential @10 mA cm^{-2} （mV）	Tafel （mV dec^{-1}）	Ref.
Rh-Co_3O_4 BNSs	0.5 M H_2SO_4	32	27.0	This work
Pure Rh	0.5 M H_2SO_4	53	42.2	This work
Co_3O_4 BNSs	0.5 M H_2SO_4	244	285	This work
RuO_2-WC NPs	0.5 M H_2SO_4	58	66	[14]
RhSiW	0.5 M H_2SO_4	46	49.9	[15]
Co-Pd-MoS_2	0.5 M H_2SO_4	49.3	43.2	[16]
PdCu/C	0.5 M H_2SO_4	40	48	[17]
N-CoP_2	0.5 M H_2SO_4	38	46	[18]
$RhSe_2$	0.5 M H_2SO_4	49.9	39	[19]
Ru-Te-C-2	0.5 M H_2SO_4	39	32	[20]
$Pt_{61}La_{39}$@KB	0.5 M H_2SO_4	38	29	[21]
CoP/Ni_2P@$Co(OH)_2$	0.5 M H_2SO_4	68	49	[22]
Ir-rEGO	0.5 M H_2SO_4	42.3	25.7	[23]
Au–Pt–Ni	0.5 M H_2SO_4	60	33	[24]

Table S2. Comparison of small-molecule-oxidation activity of catalysts with reported catalysts.

Catalyst	Electrolyte	Working potential @10 mA cm^{-2} （V vs. RHE）	Ref.
Rh-Co_3O_4 BNSs	0.5 M H_2SO_4 + 0.05 M N_2H_4	0.26	This work
Pure Rh	0.5 M H_2SO_4 + 0.05 M N_2H_4	0.36	This work
Co_3O_4 BNSs	0.5 M H_2SO_4 + 0.05 M N_2H_4	>0.70	This work
Rh_2P uNSs	0.5 M H_2SO_4 + 0.05 M N_2H_4	0.30	[25]
Rh_2S_3/NC	0.5 M H_2SO_4 + 0.1 M N_2H_4	0.53	[26]
Ir-SA/NC	0.5 M H_2SO_4+0.33 M N_2H_4	0.39	[27]
CoNiP-NIE	1 M KOH + 10 mM HMF	1.29	[28]
NiClO-D	1 M KOH + 0.33 M Urea	1.34	[29]
$NiMoP_x$@Ni_5P_4	1 M KOH + 1 M CH_3OH	1.36	[30]
Ru@MnO_{2-x}	1 M KOH + 0.5 M Glycerol	1.13	[31]

Table S3. Comparison of OHzS performance with OWS promoted by reported catalysts.

Catalyst	Electrolyte	Cell voltage @10 mA cm^{-2} (V)	Ref.
Rh-Co_3O_4 BNSs||Rh-Co_3O_4 BNSs	0.5 M H_2SO_4 + 0.05 M N_2H_4	0.34	This work
Pt/C||Pt/C	0.5 M H_2SO_4 + 0.05 M N_2H_4	0.51	This work
Rh-Co_3O_4 BNSs||Rh-Co_3O_4 BNSs	0.5 M H_2SO_4	1.72	This work
Ir@$SrIrO_3$-175||Ir@$SrIrO_3$-175	0.5 M H_2SO_4	1.49	[32]
Co-RuIr||Co-RuIr	0.1 M $HClO_4$	1.52	[33]
Rh_2P uNSs|| Rh_2P uNSs	0.5 M H_2SO_4 + 0.05 M N_2H_4	0.38	[25]
Rh_2S_3/NC|| Rh_2S_3/NC	0.5 M H_2SO_4 + 0.1 M N_2H_4	0.38	[26]
Ir-SA/NC|| Ir-SA/NC	0.5 M H_2SO_4+0.33 M N_2H_4	0.39	[27]
Rh/RhOx-500|| Rh/RhOx-500	0.5 M H_2SO_4 + 0.5 M N_2H_4	0.35	[34]
MnO_2/CP|| MnO_2/CP	0.005 M H_2SO_4+0.2 M Glycerol	1.38	[35]
Pd/$NiCo_2O_4$-2‖Pd/$NiCo_2O_4$-2	1 M KOH + 0.5 M N_2H_4	0.35	[36]
Ni─MoN/NF-6||Ni─MoN/NF-6	1 M KOH + 0.5 M Methanol & 0.5 M H_2SO_4	0.56	[37]
O-NiMoP/NF|| O-NiMoP/NF	1 M KOH + 0.5 M Urea	1.36	[38]
Co-Rh_2||Co-Rh_2	1 M KOH + 1.0 M CH_3OH	1.55	[39]
PtCu NF/C|| PtCu NF/C	1 M KOH +0.5 M Ethanol	0.58	[40]

References

1. J. Hafner, Ab-initio simulations of materials using VASP: Density-functional theory and beyond, *J. Comput. Chem.*, 2008, **29**, 2044-2078.

2. G. Kresse and J. Furthmüller, Efficient iterative schemes for ab initio total-energy calculations using a plane-wave basis set, *Phy. Rev. B*, 1996, **54**, 11169-11186.

3. G. Kresse and J. Furthmüller, Efficiency of ab-initio total energy calculations for metals and semiconductors using a plane-wave basis set, *Comput. Mater. Sci.*, 1996, **6**, 15-50.

4. P. E. Blöchl, Projector augmented-wave method, *Phys. Rev. B*, 1994, **50**, 17953-17979.

5. G. Kresse and D. Joubert, From ultrasoft pseudopotentials to the projector augmented-wave method, *Phys. Rev. B*, 1999, **59**, 1758-1775.

6. B. Hammer, L. B. Hansen and J. K. Nørskov, Improved adsorption energetics within density-functional theory using revised Perdew-Burke-Ernzerhof functionals, *Phys. Rev. B*, 1999, **59**, 7413-7421.

7. S. Grimme, S. Ehrlich and L. Goerigk, Effect of the damping function in dispersion corrected density functional theory, *J. Comput. Chem.*, 2011, **32**, 1456-1465.

8. S. L. Dudarev, G. A. Botton, S. Y. Savrasov, C. J. Humphreys and A. P. Sutton, Electron-energy-loss spectra and the structural stability of nickel oxide: An LSDA+U study, *Phys. Rev. B*, 1998, **57**, 1505-1509.

9. X. Shi, S. L. Bernasek and A. Selloni, Formation, Electronic Structure, and Defects of Ni Substituted Spinel Cobalt Oxide: a DFT+U Study, *J. Phys. Chem. C*, 2016, **120**, 14892-14898.

10. Y. G. Zhang, G. B. Zhang and Y. Xu Wang, First-principles study of the electronic structure and optical properties of Ce-doped ZnO, *J. Appl. Phys.*, 2011, **109**, 063510.

11. N. Stojić, N. Binggeli and M. Altarelli, Surface magnetism of Rh(001) fromLDA+Ucalculations, *Phys. Rev. B*, 2006, **73**, 100405.

12. J. K. Nørskov, J. Rossmeisl, A. Logadottir, L. Lindqvist, J. R. Kitchin, T. Bligaard and H. Jónsson, Origin of the Overpotential for Oxygen Reduction at a Fuel-Cell Cathode, *J. Phy. Chem. B*, 2004, **108**, 17886-17892.

13. H. A. Hansen, J. Rossmeisl and J. K. Nørskov, Surface Pourbaix diagrams and oxygen reduction activity of Pt, Ag and Ni(111) surfaces studied by DFT, *Phys. Chem. Chem. Phys.*, 2008, **10**, 3722-3730.

14. S. C. Sun, H. Jiang, Z. Y. Chen, Q. Chen, M. Y. Ma, L. Zhen, B. Song and C. Y. Xu, Bifunctional WC-Supported RuO_2 Nanoparticles for Robust Water Splitting in Acidic Media, *Angew. Chem. Int. Ed.*, 2022, **61**, e202202519.

15. D. Jeon, D. Y. Kim, H. Kim, N. Kim, C. Lee, D. H. Seo and J. Ryu, Electrochemical Evolution of Ru-Based Polyoxometalates into Si,W-Codoped RuO_x for Acidic Overall Water Splitting, *Adv. Mater.*, 2024, **36**, e2304468.

16. W. Yang, S. Zhang, Q. Chen, C. Zhang, Y. Wei, H. Jiang, Y. Lin, M. Zhao, Q. He, X. Wang, Y. Du, L. Song, S. Yang, A. Nie, X. Zou and Y. Gong, Conversion of Intercalated MoO_3 to Multi-Heteroatoms-Doped MoS_2 with High Hydrogen Evolution Activity, *Adv. Mater.*, 2020, **32**, e2001167.

17. A. Mahmood, D. He, C. Liu, S. H. Talib, B. Zhao, T. Liu, Y. He, L. Chen, D. Han and L. Niu, Unveiling the Growth Mechanism of Ordered-Phase within Multimetallic Nanoplates, *Adv. Sci.*, 2024, **11**, 2309163.

18. J. Cai, Y. Song, Y. Zang, S. Niu, Y. Wu, Y. Xie, X. Zheng, Y. Liu, Y. Lin, X. Liu, G. Wang and Y. Qian, N-induced lattice contraction generally boosts the hydrogen evolution catalysis of P-rich metal phosphides, *Sci. Adv.*, **6**, eaaw8113.

19. W. Zhong, B. Xiao, Z. Lin, Z. Wang, L. Huang, S. Shen, Q. Zhang and L. Gu, $RhSe_2$: A Superior 3D Electrocatalyst with Multiple Active Facets for Hydrogen Evolution Reaction in Both Acid and Alkaline Solutions, *Adv. Mater.*, 2021, **33**, e2007894.

20. F. Yang, Q. Wang, J. Li and L. Feng, Structural evolution of Ru/Te interaction for hydrogen generation engineered by proof of concept via carbon doping, *Mater. Today Phys.*, 2023, **38**, 101262.

21. N. Nie, D. Zhang, Z. Wang, Y. Qin, X. Zhai, B. Yang, J. Lai and L. Wang, Superfast Synthesis of Densely Packed and Ultrafine Pt-Lanthanide@KB via Solvent-Free Microwave as Efficient Hydrogen Evolution Electrocatalysts, *Small*, 2021, **17**, e2102879.

22. M. Xing, H. Liu, X. Dong, Z. Liang, S. Huang, X. Ding, L. Yang, Z. Liu, S. Wang and D. Cao, $Co(OH)_2$ promoting the catalytic activity of CoP/Ni_2P heterojunction for hydrogen evolution in both alkaline and acid media, *Mater. Today Energy*, 2022, **30**, 101142.

23. X. Li, J. Cao, J. Chen, Y. Zhu, H. Xia, Z. Xu, C. Gu, J. Xie, M. Jones, C. Lyu, J. Corbin, X. Li and W. Hu, UV-Induced Synthesis of Graphene Supported Iridium Catalyst with Multiple Active Sites for Overall Water Splitting, *Adv. Funct. Mater.*, 2024, **34**, 2313530.

24. S. Khamgaonkar, Q. Chen, K. Musselman and V. Maheshwari, Stable perovskite photocathodes

for efficient hydrogen evolution in acidic and basic conditions, *J. Mater. Chem. A*, 2023, **11**, 20079-20088.

25. Y. Zhao, N. Jia, X.-R. Wu, F.-M. Li, P. Chen, P.-J. Jin, S. Yin and Y. Chen, Rhodium phosphide ultrathin nanosheets for hydrazine oxidation boosted electrochemical water splitting, *Appl. Catal. B: Environ.*, 2020, **270**, 118880.

26. C. Zhang, H. Liu, Y. Liu, X. Liu, Y. Mi, R. Guo, J. Sun, H. Bao, J. He, Y. Qiu, J. Ren, X. Yang, J. Luo and G. Hu, Rh_2S_3/N-Doped Carbon Hybrids as pH-Universal Bifunctional Electrocatalysts for Energy-Saving Hydrogen Evolution, *Small Methods*, 2020, **4**, 2000208.

27. F. Luo, S. Pan, Y. Xie, C. Li, Y. Yu, H. Bao and Z. Yang, Hydrazine-Assisted Acidic Water Splitting Driven by Iridium Single Atoms, *Adv. Sci.*, 2023, **10**, 2305058.

28. Y. Song, W. Xie, Y. Song, H. Li, S. Li, S. Jiang, J. Y. Lee and M. Shao, Bifunctional integrated electrode for high-efficient hydrogen production coupled with 5-hydroxymethylfurfural oxidation, *Appl. Catal. B: Environ.*, 2022, **312**, 121400.

29. L. Zhang, L. Wang, H. Lin, Y. Liu, J. Ye, Y. Wen, A. Chen, L. Wang, F. Ni, Z. Zhou, S. Sun, Y. Li, B. Zhang and H. Peng, A Lattice-Oxygen-Involved Reaction Pathway to Boost Urea Oxidation, *Angew. Chem. Int. Ed.*, 2019, **58**, 16820-16825.

30. B. Zhu, J. Xiong, S. Wu, K. You, B. Sun, Y. Liu, M. Chen, P. Jin and L. Feng, Core@Shell Heterostructured $NiMoP_x$@Ni_5P_4 Nanorod Arrays Promoting Direct Electro-Oxidation of Methanol and Hydrogen Evolution under Industry Conditions, *Adv. Funct. Mater.*, 2024, 2407236.

31. H. Yu, M. Hu, C. Chen, C. Hu, Q. Li, F. Hu, S. Peng and J. Ma, Ambient gamma-Rays-Mediated Noble-Metal Deposition on Defect-Rich Manganese Oxide for Glycerol-Assisted H_2 Evolution at Industrial-Level Current Density, *Angew. Chem. Int. Ed.*, 2023, **62**, e202314569.

32. L. Zhao, Z. Tao, M. You, H. Xiao, S. Wang, W. Ma, Y. Huang, B. He and Q. Chen, Partial Exsolution Enables Superior Bifunctionality of Ir@$SrIrO_3$ for Acidic Overall Water Splitting, *Adv. Sci.*, 2024, **11**, e2309750.

33. J. Shan, T. Ling, K. Davey, Y. Zheng and S. Z. Qiao, Transition-Metal-Doped RuIr Bifunctional Nanocrystals for Overall Water Splitting in Acidic Environments, *Adv. Mater.*, 2019, **31**, e1900510.

34. J. Yang, L. Xu, W. Zhu, M. Xie, F. Liao, T. Cheng, Z. Kang and M. Shao, Rh/RhO_x nanosheets as pH-universal bifunctional catalysts for hydrazine oxidation and hydrogen evolution reactions, *J. Mater. Chem. A*, 2022, **10**, 1891-1898.

35. Y. Li, X. Wei, S. Han, L. Chen and J. Shi, MnO_2 Electrocatalysts Coordinating Alcohol Oxidation for Ultra-Durable Hydrogen and Chemical Productions in Acidic Solutions, *Angew. Chem. Int. Ed.*, 2021, **60**, 21464-21472.

36. R. A. Senthil, S. Jung, A. Min, A. Kumar, C. J. Moon, M. Singh and M. Y. Choi, Revealing the Impact of Pulsed Laser-Produced Single-Pd Nanoparticles on a Bimetallic $NiCo_2O_4$ Electrocatalyst for Energy-Saving Hydrogen Production via Hybrid Water Electrolysis, *ACS Catal.*, 2024, **14**, 3320-3335.

37. C. Rao, H. Wang, K. Chen, H. Chen, S. Ci, Q. Xu and Z. Wen, Hybrid Acid/Base Electrolytic Cell for Hydrogen Generation and Methanol Conversion Implemented by Bifunctional Ni/MoN Nanorod Electrocatalyst, *Small*, 2024, **20**, e2303300.

38. H. Jiang, M. Sun, S. Wu, B. Huang, C. S. Lee and W. Zhang, Oxygen-Incorporated NiMoP Nanotube Arrays as Efficient Bifunctional Electrocatalysts For Urea-Assisted Energy-Saving Hydrogen Production in Alkaline Electrolyte, *Adv. Funct. Mater.*, 2021, **31**, 2104951.

39. Y. Guo, X. Yang, X. Liu, X. Tong and N. Yang, Coupling Methanol Oxidation with Hydrogen Evolution on Bifunctional Co-Doped Rh Electrocatalyst for Efficient Hydrogen Generation, *Adv. Funct. Mater.*, 2022, **33**, 2209134.

40. H. Fu, N. Zhang, F. Lai, L. Zhang, S. Chen, H. Li, K. Jiang, T. Zhu, F. Xu and T. Liu, Surface-Regulated Platinum–Copper Nanoframes in Electrochemical Reforming of Ethanol for Efficient Hydrogen Production, *ACS Catal.*, 2022, **12**, 11402-11411.